Constitutive Behavior of Commercial Grade ZEK100 Magnesium Alloy Sheet over a Wide Range of Strain Rates

SRIHARI KURUKURI, MICHAEL J. WORSWICK, ALEXANDER BARDELCIK, RAJA K. MISHRA, and JON T. CARTER

The constitutive behavior of a rare-earth magnesium alloy ZEK100 rolled sheet is studied at room temperature over a wide range of strain rates. This alloy displays a weakened basal texture compared to conventional AZ31B sheet which leads to increased ductility; however, a strong orientation dependency persists. An interesting feature of the ZEK100 behavior is twinning at first yield under transverse direction (TD) tensile loading that is not seen in AZ31B. The subsequent work hardening behavior is shown to be stronger in the TD when compared to the rolling and 45 deg directions. One particularly striking feature of this alloy is a significant dependency of the strain rate sensitivity on orientation. The yield strength under compressive loading in all directions and under tensile loading in the TD direction is controlled by twinning and is rate insensitive. In contrast, the yield strength under rolling direction tensile loading is controlled by non-basal slip and is strongly rate sensitive. The cause of the in-plane anisotropy in terms of both strength and strain rate sensitivity is attributed to the initial crystallographic texture and operative deformation mechanisms as confirmed by measurements of deformed texture. Rate-sensitive constitutive fits are provided of the tensile stress–strain curves to the Zerilli–Armstrong[1] hcp material model and of the compressive response to a new constitutive equation due to Kurukuri *et al.*[2]

DOI: 10.1007/s11661-014-2300-7

I. INTRODUCTION

MAGNESIUM alloys have attracted increased attention in recent years as lightweight materials for the transportation industry. Indeed, the low density of magnesium and its relatively high specific strength make it an excellent candidate for applications where reduction of structural weight and fuel consumption are common challenges. However, present applications of magnesium alloys are mostly limited to extruded and cast parts[3] since magnesium sheet alloys have limited formability at room temperature.[4] The limited formability is due to the hexagonal close-packed (hcp) structure of magnesium alloys, such as AZ31B sheet, which offers only a limited number of slip systems that are active at room temperature due to the strong basal crystallographic texture.[5,6] The formability can be increased by forming at elevated temperatures[7–10]; however, warm forming requires more complex tooling and lubrication strategies which increase the cost of the forming operation.

One of the techniques used to improve the room temperature formability of magnesium alloys is the addition of rare-earth elements such as Ce, Nd, Y, and Gd, for example, which have been shown to weaken the basal texture.[11–16] Rare-earth addition modifies and weakens the basal texture of a rolled Mg alloy, resulting in an enhancement of formability as well as reduced mechanical anisotropy at room temperature. Bohlen *et al.*[11] investigated the rolling texture and anisotropy of several Mg-Zn alloy sheets with different levels of Zn and rare-earth additions. They reported that the overall texture strength and the basal pole intensity aligned with the sheet normal direction was lower for rare-earth containing alloys than for conventional alloys. The anisotropy of the yield and flow strengths was reversed in comparison to conventional alloys, and the planar anisotropy or Lankford coefficient (R value) was reduced to unity. These changes were related to the fact that the dominant texture components in the rare-earth Mg-Zn alloys placed more grains in favorable orientations for basal slip and tensile twinning. Al-Samman and Li[16] studied texture modifications in Mg alloys due to rare-earth additions such as Gd, Nd, Ce, La and found that different rare-earth elements have different solid solubility and give rise to distinct microstructures. Mg alloy sheets with La, Nd, Gd have less anisotropy and ductility than those with Ce. The R value for all of the Mg-Zn rare-earth sheets tested was around 1.0 except the Mg-Zn-Ce sheet whose R values ranged from 1.2 in the rolling direction (RD) to 1.7 in the transverse direction (TD) (compared to 2.2 to 4.0 for typical commercial AZ31B sheet). The improved texture of

SRIHARI KURUKURI, Postdoctoral Researcher, MICHAEL J. WORSWICK, Professor, Tier 1 Canada Research Chair, and ALEXANDER BARDELCIK, Research Associate, are with the Department of Mechanical & Mechatronics Engineering, University of Waterloo, 200 University Avenue West, Waterloo, Ontario N2L 3G1, Canada. Contact e-mail: srihari.kurukuri@uwaterloo.ca RAJA K. MISHRA, Technical Fellow, and JON T. CARTER, Staff Researcher, are with Chemical and Materials Systems Laboratory, General Motors R & D, Warren, MI 48090.

Manuscript submitted August 2, 2013.
Article published online April 16, 2014

rare-earth alloyed ZEK100 sheet has been shown to lead to enhanced formability relative to AZ31B, as demonstrated by Boba *et al.*[10] In particular, ZEK100 was shown to form successfully at temperatures considerably lower than those required for AZ31B.

To support the introduction of magnesium alloys into vehicle body structures, the dynamic behavior of magnesium alloys must be determined to assess their likely performance during a crash event.[17,18] Extensive research has been carried out on the plastic deformation behavior of magnesium alloys, but most studies have focused on quasi-static loading conditions.[5,6,8] The high strain rate behavior is of great interest to the automotive and aircraft industries since the dynamic response of components must be known to support design and simulation for severe loading conditions, such as crash or impact. Upon impact, the local strain rates are high within the collapsing sections of impacted structures, underlying the importance of accounting for the material's strain rate sensitivity when numerically simulating these events.[18,19] Moreover, in some innovative metalworking methods, such as electromagnetic forming or explosive forming, materials undergo large amounts of strain at high rates of strain (in excess of 10^3 s^{-1}) as reported by Imbert and Worswick[20,21] and for aluminum and magnesium alloy sheets.[22] Yokoyama[23] studied the dynamic response of magnesium alloys without any remarkable increase in elongation for extruded AZ31B alloy, although the absorbed energy at high strain rates improved. Mukai *et al.*[24] also investigated the influence of grain size and observed that the tensile strength and ductility of magnesium alloys increased at high strain rates. El-Magd and Abouridouane[25] reported an increase in ductility for extruded AZ80 magnesium alloy under dynamic compressive loading. However most of these high strain rate studies have concentrated on extruded magnesium alloys which usually have a different initial crystallographic texture compared to rolled sheets. Recently, Ulacia *et al.*[19] studied the constitutive behavior of commercial magnesium alloy AZ31B rolled sheet at high strain rates. They observed that the flow stress and also elongation increase considerably at high strain rates when compared with quasi-static rates resulting in an increase in energy absorption. Hasenpouth[18] also studied the tensile behavior of AZ31B rolled sheet at different orientations over a wide range of strain rates and observed that the material shows significant positive strain rate sensitivity and moderate in-plane anisotropy over the complete range of strain rates. Kurukuri *et al.*[2] characterized the response of AZ31B sheet under both tensile and compressive loading over a wide range of strain rates. Under tensile loading, they found that the yield strength was strongly rate sensitive whereas the rate of work hardening was relatively rate insensitive for all in-plane loading orientations. Under compressive loading, AZ31B retained its characteristic sigmoidal stress–strain curve at all strain rates. The initial compressive yield stress, which is dominated by twinning response, was rate insensitive whereas subsequent hardening rate was strongly rate sensitive. Kurukuri *et al.*[2] developed a new constitutive equation that captured the sigmoidal shape of the uniaxial stress–strain and observed strain rate sensitivity.

In the present work, the room temperature constitutive behavior of 1.6-mm-thick rare-earth magnesium alloy ZEK100 rolled sheet, measured in terms of the stress–strain response, the Lankford parameter (R value) and strain rate sensitivity, along different sheet and loading orientations is characterized over a wide range of strain rates. In order to determine the anisotropy and asymmetry of the mechanical properties, tensile tests are performed in the rolling and TDs and at 45 deg to the rolling direction (designated herein as RD, TD, and 45 deg, respectively) and compression tests are performed in the rolling, transverse, and through-thickness (TT) directions. Adhesively bonded stacked sheet specimens were utilized for compressive testing, which delayed buckling during testing. In addition to the mechanical characterization effort, this study also includes detailed characterization of texture evolution under tensile and compressive loading after final deformation. The coupling between mechanical response and the crystallographic texture is identified and discussed in light of known deformation mechanisms operating at different orientations and strain rates. A new rate-sensitive constitutive model is proposed to capture the compressive behavior of this alloy, with its characteristic sigmoidal hardening response. The tensile behavior is fit to the well-known Zerilli–Armstrong rate-sensitive constitutive model[1] for hcp alloys.

II. EXPERIMENTAL METHODS

A. *Material*

A rolled rare-earth magnesium alloy sheet, ZEK100 (1.3 wt pct Zn, 0.2 wt pct Nd, 0.25 wt pct Zr and 0.01 wt pct Mn) was used in this study in an as-fabricated or F-temper condition. The nominal thickness of the sheet is 1.6 mm and the pole figure of initial texture is shown in Figure 1. EBSD data was obtained using a LEO 1450 scanning electron microscope (SEM) fitted with a TSL EBSD camera. The EBSD data was analyzed using the TSL™ OIM software (Ver. 4.6). The data was cleaned to remove bad data points and only data points having a confidence index (CI) above 0.2 were retained for the analyses. EBSD data was also taken from deformed sample surfaces normal to the loading axis. From the basal and prismatic pole figures presented in Figure 1, the ZEK100 sheet exhibits relatively weak basal texture, with significant spreading in the TD and a weak peak intensity that is about one-fourth of that of typical commercial AZ31B rolled sheet as reported by Kurukuri *et al.*[2]

B. *Specimen Preparation*

Uniaxial tensile tests were performed over a range of nominal strain rates, from 0.001 to 1000 s^{-1}, utilizing the miniature dog-bone specimens described by Smerd *et al.*[26] with a short gauge length, shown in Figure 2(a).

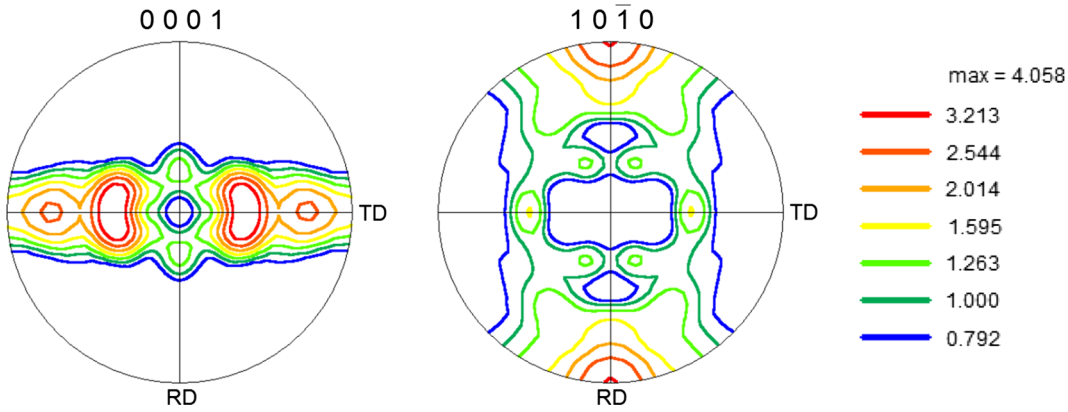

Fig. 1—Texture plot from ZEK100 sheet surface showing the majority of grains to have their *c*-axes oriented normal to the rolling direction (RD) and at an angle tilted from the sheet normal along the transverse direction (TD). Note that the intensity maxima of the prism planes show them to be normal to the RD.

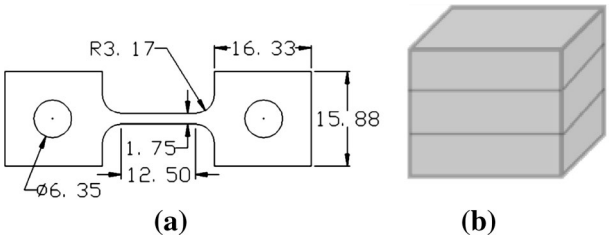

Fig. 2—(*a*) Tensile miniature dog-bone and (*b*) compression stacked sheet (4.5 × 4.5 × 4.5) samples used in this work (dimensions in mm).

To avoid any geometrical effect from one test to another, the same sample geometry was used for tests at all strain rates. This sample has a gauge length of 12.5 mm and is 1.75 mm wide, which is small enough to ensure dynamic equilibrium during high-rate experiments. Furthermore, this specimen geometry has been shown to produce stress–strain data matched to that of standard ASTM tensile specimens up to the ultimate tensile stress (UTS) for different materials, such as aluminum,[26] advanced high strength steels,[27] and AZ31B magnesium sheet.[17] This correlation is acceptable since only the flow stress up to UTS is utilized in constitutive modeling in order to ensure uniaxial conditions. The reader is cautioned that the post uniform elongation will differ between the current miniature samples and a longer gauge length ASTM sample. The effect of anisotropy of the sheet material on mechanical behavior was studied by performing tests along the rolling, transverse, and 45 deg orientations with respect to the sheet rolling direction, referred to as the RD, TD, and 45 deg directions, respectively.

The experimental characterization in uniaxial compression loading is well established for bulk materials. For sheet metal testing under uniaxial compressive loading, the geometry of the specimen plays an important role, since the thickness of the material is small compared to the other dimensions. In the current compressive experiments, adhesively bonded sheet laminates, as shown in Figure 2(b), were prepared in order to delay the onset of buckling during testing.[28,29] A structural adhesive material, Master Bond Supreme 10HT, was used to bond the sheets into cubes which could be tested over a wide range of strain rates. To improve the performance of the adhesive, the bonding surface of each sheet was roughened by light machining. It is essential to take care that each sheet blank in the laminate is oriented in the same direction with respect to the rolling direction since the samples were used for characterizing the in-plane anisotropy of the material. The effects of sample size, different adhesive materials used for stacking and different lubrication conditions between interfaces have been studied and presented elsewhere.[28] In that work, it was determined that the specimens deform in a uniform manner until the onset of shear or buckling instability beyond which the data was discarded. Before testing, the surfaces which were in contact with the incident and transmitter bar were ground and polished using three different grades of emery papers (500, 1200, and 4000 grit) to keep the friction low and also to avoid any damage to the incident and transmitter bar contact surfaces. While testing, an oil-based lubricant, Krytox [perfluoropolyether (PFPE)-based oil with polytetrafluoroethylene (PTFE) powder], was used to reduce the friction between the contact faces of the tested sample and the apparatus.

C. *Mechanical Testing*

The quasi-static (0.001, 0.01, and 0.1 s^{-1}) tensile experiments were performed using a servo-hydraulic Instron (Model 1331) tensile testing machine. Specimen elongation was measured using a 12.5 mm gauge length (±5 mm span) extensometer manufactured by Instron as shown in Figure 3(a). The intermediate strain rate (1, 10, and 100 s^{-1}) tensile experiments were conducted using a hydraulic intermediate strain rate (HISR) apparatus. A photograph of the HISR is shown in Figure 3(b). An enhanced laser displacement system (ELDS) was used to measure the specimen elongation; a detailed description of this apparatus can be found in Bardelcik *et al.*[30] High strain rate tensile tests at nominal strain rate of

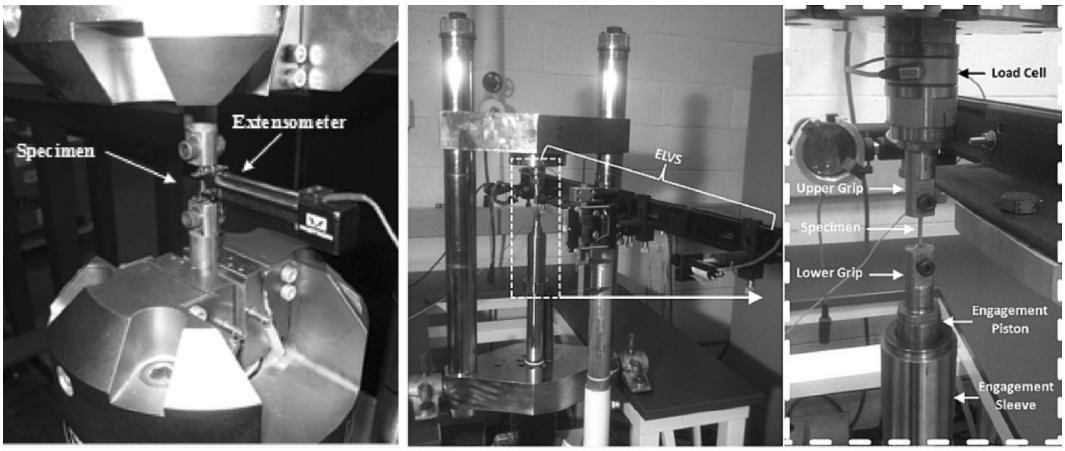

(a) QS tensile test apparatus (b) Hydraulic intermediate strain rate apparatus

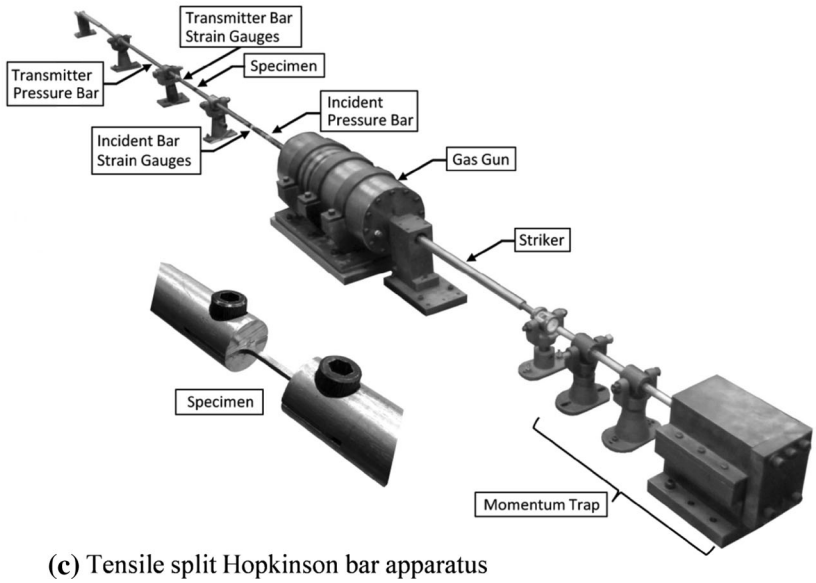

(c) Tensile split Hopkinson bar apparatus

Fig. 3—Equipment used for tensile testing.

1000 s^{-1} were performed using a tensile split Hopkinson bar (TSHB) apparatus shown in Figure 3(c). Strain gauges mounted on the incident and transmission bar were used to measure the specimen elongation. A detailed description of the equipment and procedures used to calculate the engineering stress and strain data can be found elsewhere.[26,27,31,32] Table I summarizes the mechanical test conducted in this study.

The experimental setup for the low rate uniaxial compression testing is shown in Figures 4(a) and (b). In this work, a custom compression test fixture was mounted within the Instron apparatus. This fixture mounts the compression platens within a die set to maintain accurate alignment during testing. Before placing the sample between the platens, the contact faces of the platens were cleaned with acetone. The cross-head velocity was set to 0.0047 and 0.047 mm s^{-1} to deform the specimen at nominal strain rates of 0.001 and 0.01 s^{-1}, respectively. Strain measurement was done with a digital image correlation (DIC) system. The high strain rate compression experiments were conducted using the compressive split Hopkinson bar (CSHB) apparatus described by Mason and Worswick.[33] The CSHB apparatus is presented in Figure 4(c) and a detailed description of the procedures used to calculate the engineering stress and strain data can be found in Salisbury.[31]

Table I. Summary of Test Methods

	Apparatus/Extensometer	Strain Rate
Tension	Instron/12.5 mm clip-on	0.001, 0.01, and 0.1 s^{-1}
	HISR/18.86 mm non-contact	1, 10, and 100 s^{-1}
	TSHB/strain gauges	1000 s^{-1}
Compression	Instron—compression rig/DIC	0.001 and 0.01 s^{-1}
	CSHB/strain gauges	1000 s^{-1}

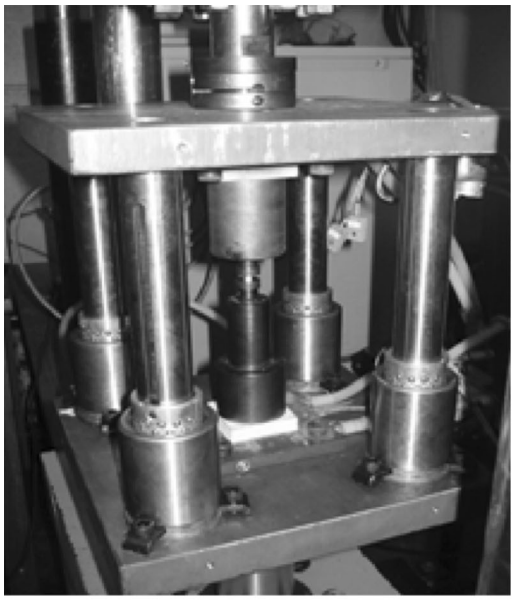

(a) QS compression test rig

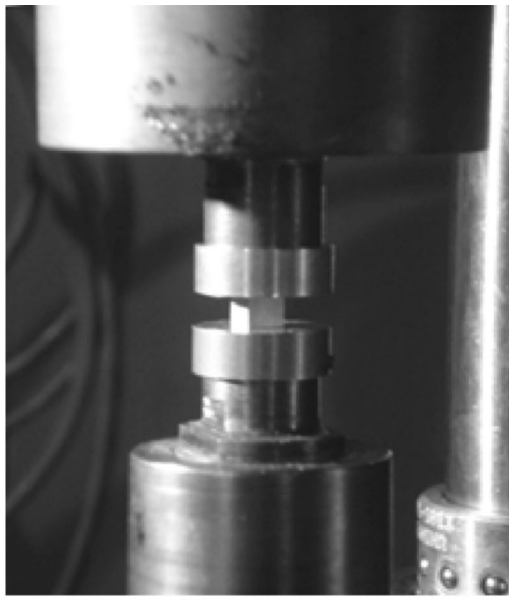

(b) Stacked sample in test rig

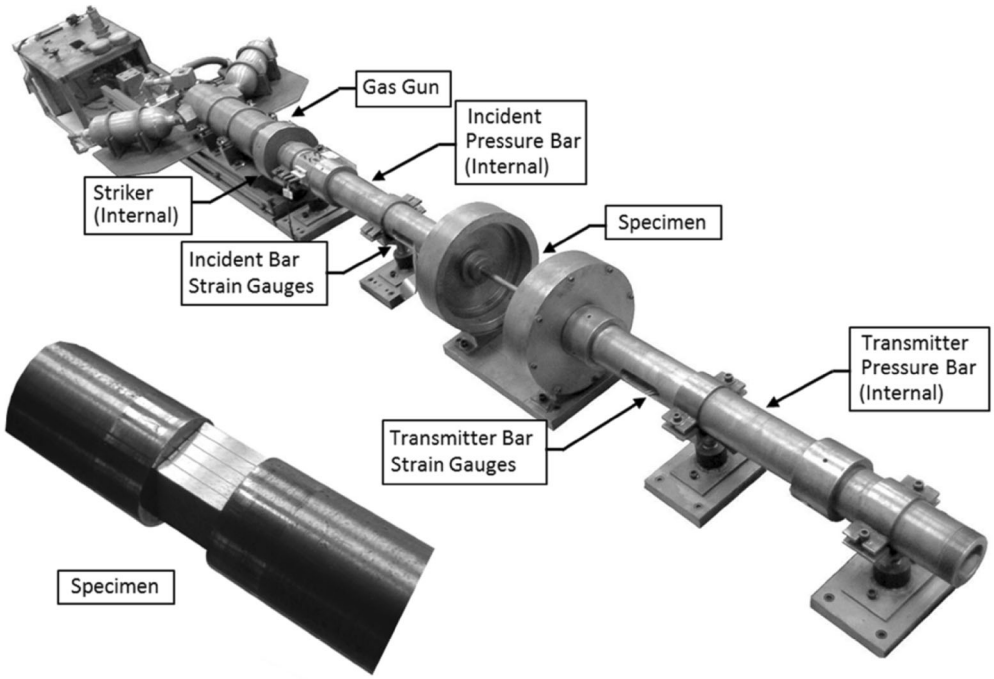

(c) Compression split Hopkinson bar apparatus

Fig. 4—Equipment used for compression testing.

D. *Strain Measurement in HISR and TSHB*

It is important to note a difference in the manner in which strain measurements were performed on the HISR and TSHB in contrast to the strain measurements performed on the Instron test apparatus used in this work. The difference lies primarily in the gauge length over which the elongation is measured. The Instron tests utilize a clip-on extensometer which has a gauge length of 12.5 mm as shown in Figures 2(a) and 3(a). However, there is no "dynamic extensometer" for the HISR apparatus; instead, these experiments utilize a contactless extensometer which measures the extension across the specimen shoulders corresponding to an initial length of 18.86 mm and therefore also measures deformation that occurs outside of the 12.5 mm gauge length region of the sample. The TSHB method[26,27,31,32] measures the displacements at the bar ends which is equivalent to the measure of displacement in the HISR

experiments. This difference in specimen elongation measurement introduces additional deformation (primarily elastic) from outside the gauge length that is measured and when converted to engineering strain, results in a lower apparent Young's modulus.[30] To compensate for these different gauge lengths, an "apparent modulus" is calculated for each experiment and used in the calculation of effective plastic strain. Following Bardelcik *et al.*,[30] this approach serves to compensate for the different elongation measurements and provides a measure of effective plastic strain that is relatively insensitive to the manner in which elongation is measured. Recent work by Bardelcik[34] has shown that that the true stress *vs* effective plastic strain response determined using the current technique (based on the measured elongation between the specimen shoulders) agrees well with that determined using high speed DIC strain measurements taken directly from the sample gauge region.

III. MECHANICAL CHARACTERIZATION RESULTS

A. *Effect of Strain Rate on the Tensile Flow Stress*

The influence of strain rate on the tensile flow stress behavior of ZEK100 sheet can be seen in Figure 5, in which the flow curves at different strain rates are plotted for the RD, TD, and 45 deg orientation, respectively. In the RD, there is a clear increase of the yield strength as the strain rate increases, as shown in Figure 5(a). Over the entire range of strain rates considered, the yield strength level increased by approximately 75 MPa for the RD, which represents an increase of 25 pct. It is reported in the literature that for tension tests on AZ31B in the RD; non-basal slip systems were generally activated, since basal planes are unfavorably oriented for slip in most of the grains.[4,11,35] Such deformation behavior is typically observed for AZ31B rolled sheet, irrespective of sheet orientation.[4,35] Thus, the increase in tensile yield stress with an increase in strain rate can mainly be attributed to strain rate dependency of the CRSS of non-basal slip systems. This behavior is commonly observed in typical commercial rolled AZ31B sheet.[2,4,35]

The transverse tensile data (Figure 5(b)) for the ZEK100 sheet shows very different behavior compared to the RD results. The TD yield stress is strain rate insensitive, but the work hardening rate increases for higher rates of loading. This yield strength rate-insensitivity is due to the strain rate independency of the CRSS of basal slip systems and the extension twinning mechanisms activated during the early stages of deformation in the grains for which the crystallographic *c*-axes are oriented toward the TD.[35,36] The rate sensitivity of the TD work hardening rate is attributed to the rate dependency of non-basal slip activated during the later stages of deformation.[5,11,35–37] Figure 5(c) illustrates the flow curves corresponding to the tensile tests carried out on ZEK100 samples along the 45 deg orientation. The 45 deg samples exhibit moderate strain rate dependency of yield strength and work hardening rates compared to the TD samples.

B. *Effect of In-plane Orientation on the Tensile Flow Stress at Different Strain Rates*

The true stress *vs* plastic strain curves in the RD, TD, and 45 deg direction for the quasi-static strain rate tensile experiments are shown in Figure 6. It is seen from the flow stress–plastic strain data presented in Figure 6 that the ZEK100 sheet exhibits strong in-plane anisotropy with the yield strength being the lowest in the TD and highest in the RD at all strain rates. The flow stress for the specimens oriented along 45 deg falls between the TD and RD data at low strain levels. The work hardening rates are also dramatically different for the three material directions, with the lowest hardening occurring along the RD. The data for the TD and 45 deg orientation overlaps at a strain of roughly 0.12 (for example, see Figure 6). Note that, similar trends were observed at all other strain rates.

C. *Compressive Response of ZEK100 Sheet at Different Strain Rates and Orientations*

The curves presented in Figure 7 illustrate the flow stress–strain data corresponding to uniaxial compression tests carried out at quasi-static and dynamic strain rates until failure along the RD, TD, 45 deg and TT. The stress–strain behavior is clearly dependent on the load orientation with respect to the rolling direction of the polycrystalline aggregate, suggesting different deformation mechanisms are activated in each of the three orientations investigated. From Figure 7(a), it is observed that the shape of the stress–strain curves is concave upwards (S-shape) in the rolling direction at all strain rates and such a stress–strain response is consistent with the predominance of {10-12} twinning at low strains, followed by strong strain hardening at large strains, as typically observed for commercial AZ31B rolled sheet.[2,4,35] When loaded along the TD (Figure 7(b)) and in the 45 deg deformation direction (Figure 7(c)), the ZEK100 sheet exhibits a lower stress level for a given strain compared to the rolling direction. The TT compressive true stress–plastic strain curves (Figure 7(d)) tend more toward a concave downward shape, reflecting a predominant crystallographic slip deformation mechanism and weaker contraction twinning effects, which is consistent with trends reported in the literature for AZ31B.[2,5,11,35,37,38] When comparing the effect of strain rate on the compressive response, the stresses in the twinning regime (strains less than 4 pct) are strain rate independent whereas in the subsequent crystallographic slip regime (strains greater than 4 pct) the flow stress response shows strong strain rate sensitivity in all in-plane loading directions (Figure 7). The TT tests exhibits very mild strain rate sensitivity in terms of the initial yield strength, but the work hardening rate increases for higher rates of loading.

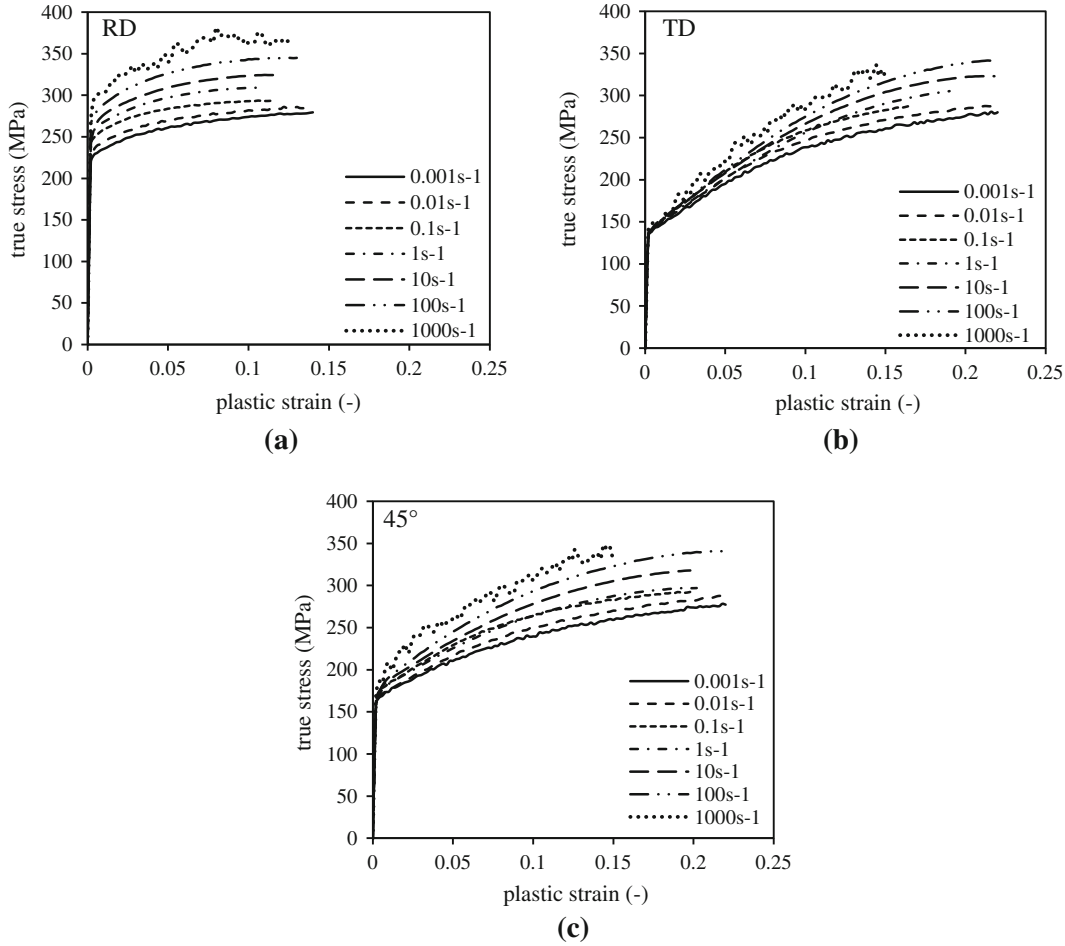

Fig. 5—Effect of strain rate on the tensile flow curves of ZEK100 sheet in different orientations and strain rates.

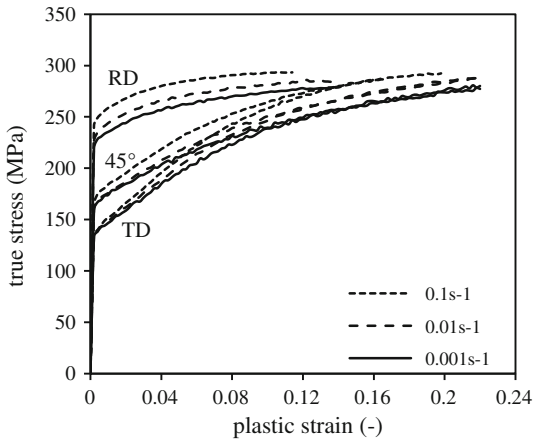

Fig. 6—Effect of sheet orientation on the tensile behavior of ZEK100 sheet.

D. *Tension–Compression Asymmetry of ZEK100 Sheet*

Figure 8(a) compares the true stress–effective plastic strain curves for ZEK100 sheet deformed in in-plane tension and compression at dynamic strain rates ($1000\ s^{-1}$) along the RD and TD, respectively. In the rolling direction, the shape of the flow curve is concave down under tensile loading and concave up under compressive loading, similar to the shape of the curves commonly observed in typical commercial AZ31B rolled sheet.[2,4,35] These distinct shapes are consistent with the predominance of crystallographic slip in tension and of {10-12} twinning followed by rapid work hardening due to non-basal crystallographic slip in compression.[4,5,35] The yield stress for in-plane compression along the RD is approximately one-half of the yield stress in tension. On the other hand, the ZEK100 sheet exhibits a lower stress level for a given strain in the TD compared to the RD for both tension and compression loading. It is interesting to note that the asymmetry in the yield stress is minimal in the TD compared to the strong asymmetry observed in the RD.

Figure 8(b) shows the variation of work hardening rate $\left(d\bar{\sigma}/d\bar{\varepsilon}_p\right)$ corresponding to the flow curves presented in Figure 8(a) for the in-plane tension and compression tests in the RD and TD at dynamic strain rates. The measured work hardening rate under tensile and compressive loading reveals a significant change in work hardening rate with loading orientation. For example, under tensile loading at a true strain of 4 pct, the work hardening rate in the RD is approximately 1000 MPa whereas the TD orientation exhibits a work hardening rate of 1550 MPa, respectively. The

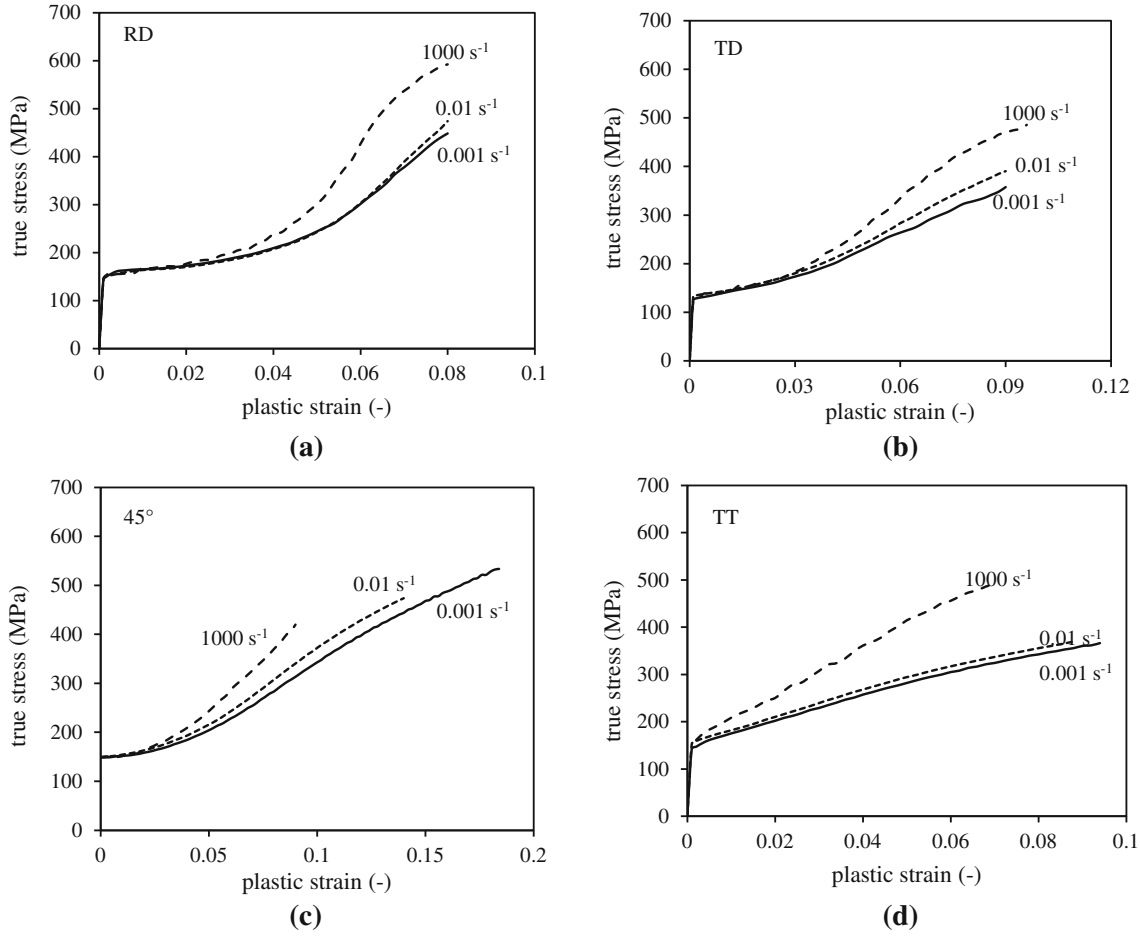

Fig. 7—Effect of strain rate on the compressive flow curves of ZEK100 sheet in different orientations.

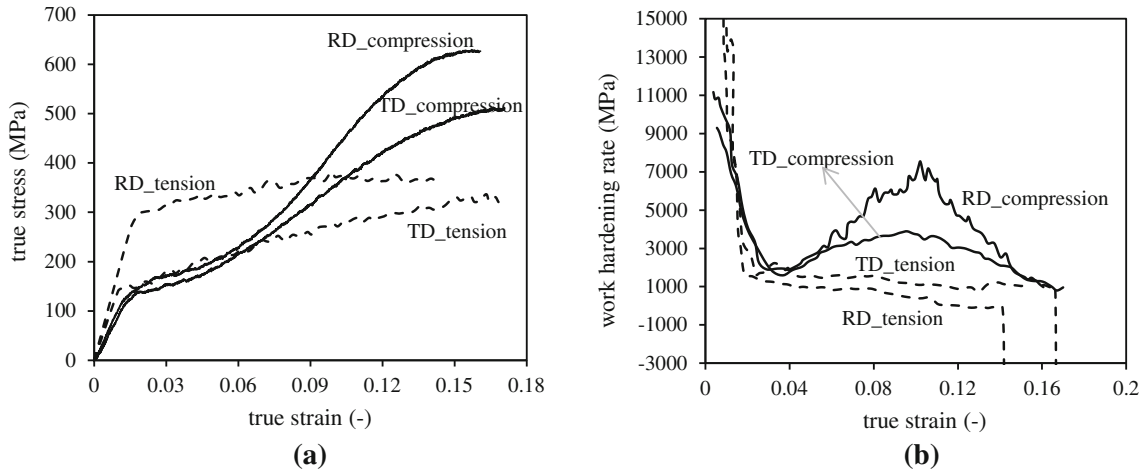

Fig. 8—Tension–compression asymmetry of (*a*) flow curves and (*b*) their corresponding work hardening rates in different orientations at a strain rate of 1000 s^{-1}.

hardening rates in the tensile samples show monotonic decrease with strain. For the RD and TD compressive loading, the hardening rate in the twinning regime (strains less than 4 pct) is nearly directionally independent whereas in the subsequent crystallographic slip regime (strains greater than 4 pct) the hardening rate is much higher for the RD samples than in the TD samples.

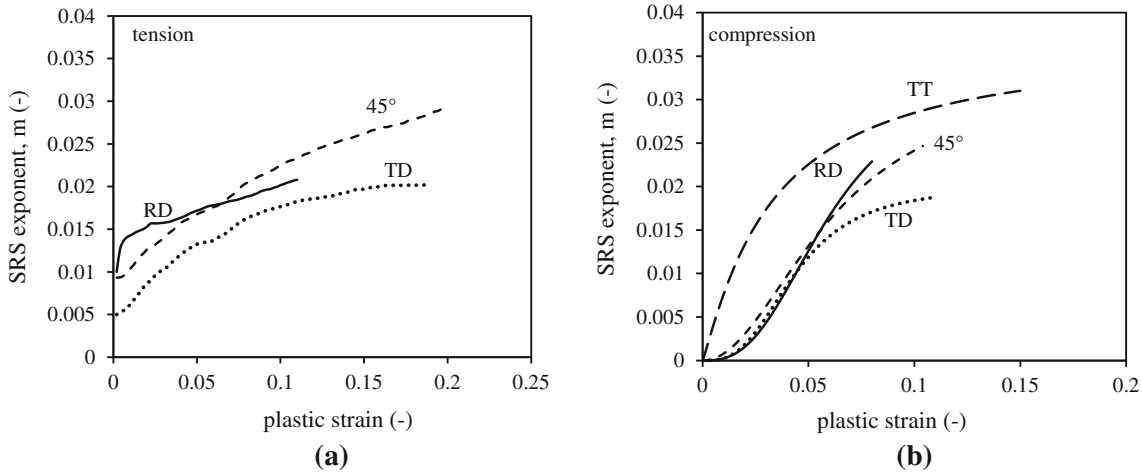

Fig. 9—Strain rate sensitivity *vs* plastic strain at a strain rate of 0.001 s^{-1}.

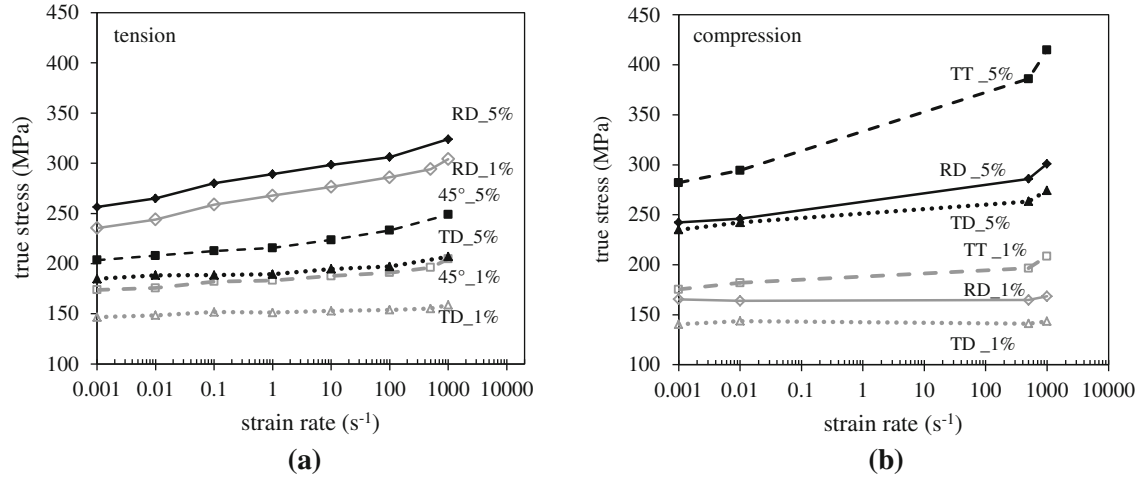

Fig. 10—Strain rate effects under tension and compression in different orientations.

E. *Strain Rate Sensitivity*

The strain rate sensitivity (SRS) index calculated from the relation, $m = \partial \ln \bar{\sigma} / \partial \ln \dot{\varepsilon}_p$, as a function of plastic strain is plotted in Figure 9 for the RD, TD, and 45 deg in-plane tension and compression and TT compression at a strain rate of 0.001 s^{-1}. Under tensile loading (Figure 9(a)), the material clearly exhibits positive strain rate sensitivity in all directions and loading paths, with the SRS being lowest in the TD at all strain levels. On the other hand, when compressing the sample in the in-plane direction (Figure 9(b)), the SRS is almost zero during the early stages of deformation which is twinning dominated. At higher strains, the strain rate sensitivity recovers as conventional crystallographic slip is established and the TD direction again shows the lowest SRS.

Figure 10(a) illustrates the tensile true stress data at 1 and 5 pct effective plastic strain, respectively, as a function of strain rate (logarithmic scale) for the ZEK100 sheet in the RD, TD, and 45 deg orientations. The flow stress in the transverse and 45 deg directions exhibits almost no strain rate sensitivity at low strains (at 1 pct strain, shown in Figure 8(a)), whereas the rate sensitivity at higher strain (at 5 pct strain) is much higher. In contrast, the flow stress data in the rolling direction exhibits pronounced rate sensitivity over the entire strain range. Similarly, Figure 10(b) illustrates the compressive true stress at 1 and 5 pct effective plastic strain as a function of strain rate (logarithmic scale) for the ZEK100 sheet in the RD, TD, and TT orientations. The flow stress in the rolling and TDs exhibits no rate sensitivity at low (1 pct) strain; whereas the rate sensitivity increases at higher (5 pct) strain. The flow stress in the TT direction exhibits moderate rate sensitivity at low strain and very pronounced rate sensitivity at higher strain. From Figure 10, it can also be seen that the degree of tension–compression asymmetry will increase with strain rate, primarily at lower strain levels in the RD, whereas in the TD, the degree of tension–compression asymmetry is mild at low strain levels.

F. *Anisotropy of Deformation*

Another important parameter measured during uniaxial testing is the Lankford coefficient or *R* value,

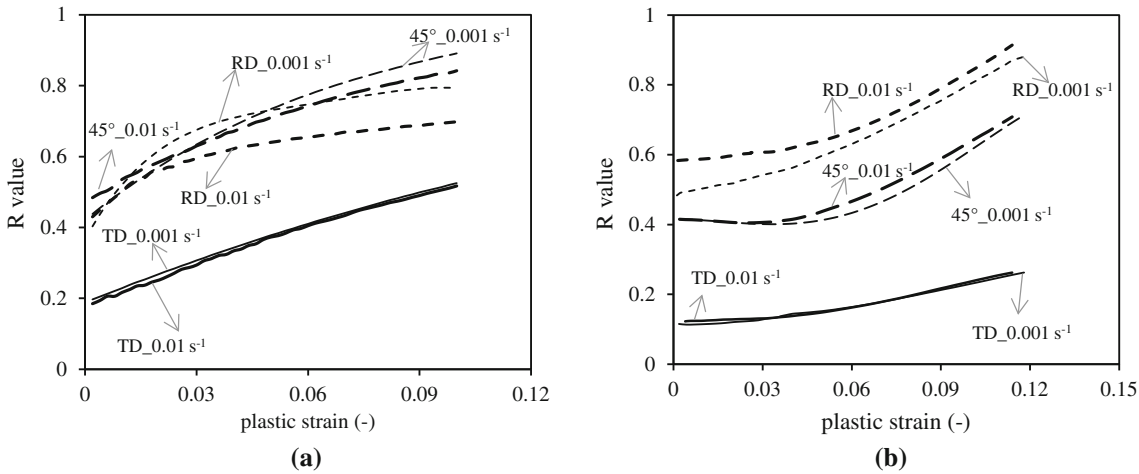

Fig. 11—Evolution of instantaneous R values in different orientations and strain rates in (*a*) tension and (*b*) compression.

defined as the ratio of the width strain to the thickness strain. The instantaneous R values measured at room temperature in different orientations along the tensile and compressive loading directions at strain rates of 0.001 and 0.01 s^{-1} are plotted in Figure 11. In general, the measured R values for TD loading in both tension and compression are much lower than observed for the RD and 45 degree orientations. This trend can be attributed to greater resistance to in-plane deformation along the RD *vs* TT direction which is a direct result of the spread of the basal texture along the TD direction seen in Figure 1.[6,39] It can be clearly seen that, unlike the R values for many fcc and bcc metals, the R value for magnesium alloy sheet evolves with plastic deformation. However, the extent of R value evolution is considerably less than that reported by Kurukuri *et al.*[2] for AZ31B and the R values measured here for ZEK100 are much closer to unity than for AZ31B. The effect of strain rate on R value is seen to be mild.

IV. TEXTURE EVOLUTION

Figure 12 shows the comparison of texture plots (basal and prismatic pole figures) of samples before and after tensile deformation along the RD at a strain rate of 0.01 and 100 s^{-1}. The initial sample has essentially no *c*-axis poles parallel to the RD and the loading axis and this does not change with tensile deformation. The position and intensities of the basal poles in the deformed samples are similar with a slight enhancement of the intensity maxima value in the 100 s^{-1} sample. However the basal pole positions are smeared around the TD pole in the deformed samples and the prism plane pole is strengthened. The low hardening rates in Figure 5(a) and the texture plots suggest that very little twinning occurs in these samples; deformation being accommodated mainly by slip. The rotation of the prism planes is indicative of dislocation activity in the prism plane. The high value of yield stress and its dependence on strain rate (Figure 5(a)) can be interpreted as yielding occurring by the activation of prismatic dislocations rather than basal dislocations (whose CRSS is generally very low).

Figure 13 serves to compare the measured textures from an undeformed sample with that of deformed samples pulled in the TD at strain rates of 0.01 and 100 s^{-1}. The data shows that major reorientation of the lattice takes place during deformation. Those grains with their *c*-axes parallel to the TD seem to have rotated away by extension twinning to lie along the TT and RD which are under compression and this is more prominent at higher strain rate compared to lower strain rate. The weakening of the texture intensity from the 0.01 s^{-1} sample to the 100 s^{-1} sample and the position of the prism plane intensities suggest that the strengthening of the material after initial yield is by slip on the prismatic and pyramidal planes while the yield stress is dominated by the activation of twinning. The stress–strain curves in Figure 5(b) show a slight S-shape in the TD tensile samples compared to the RD tensile samples. Furthermore, twinning is a rate-independent process, thus the yield stress of the TD tensile samples does not change with strain rate, unlike the RD tensile samples. However, the strain rate affects slip activity following yield and increased interaction between basal and prismatic dislocations (as well as pyramidal ones) leads to high strain hardening that is rate sensitive.

Figure 14 shows the pole figures of the deformed compression samples along the RD, TD, and TT directions at a strain rate of 0.01 s^{-1}. It is clear from the pole figures in Figure 14 that, in all the compression samples, irrespective of the orientation, the *c*-axes of the grains rotate to lie parallel to the compression axis. This is typically the case when Mg deforms by extension twinning. For the sample compressed along the RD, the undeformed material has all of the grains with their *c*-axes normal to the RD and they all undergo extension twinning. The strong S curve seen in Figure 7(a) is consistent with this observation. The amount of twinning in the TD and TT compression samples is less, reflected in the spread of the basal pole intensity along the TT and TD. A smaller fraction of grains that have *c*-axes normal to the compression axis in these samples

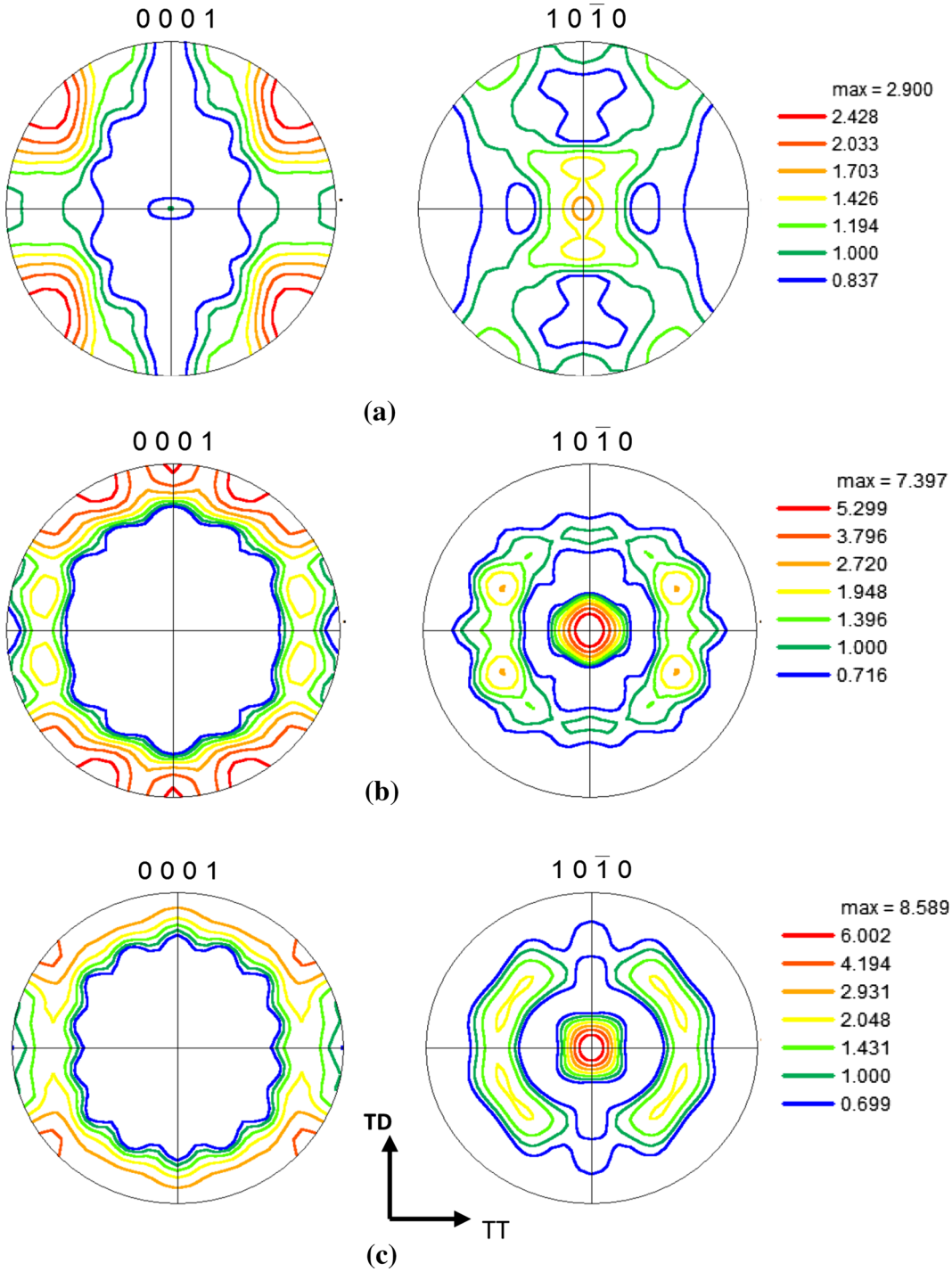

Fig. 12—Texture plots (0001) (left) and (10$\bar{1}$0) (right) of (*a*) undeformed sample, and samples deformed along the RD until failure at a strain rate of (*b*) 0.01 s^{-1}, (*c*) 100 s^{-1}. Samples examined with the electron beam parallel to RD. Axis system indicates sheet orientation.

will be deformed by extension twinning and further deformation will be accompanied by slip. The location of intensity maxima in the TD and TT samples suggest predominantly prismatic slip in the former with pyramidal slip in the latter. Samples deformed at higher strain rates show the same behavior, with slight differences in the intensities of the poles (not shown here for brevity).

The texture plots also show that yielding in the compression samples and tensile sample deformed along the TD is determined by the onset of twinning—the values of yield stress are the same in all cases and are rate insensitive. The strain rate sensitivity in the TT compression sample in Figure 9(b) indicates the slip activity in this sample to be different from that in the RD and TD compression samples, most likely a

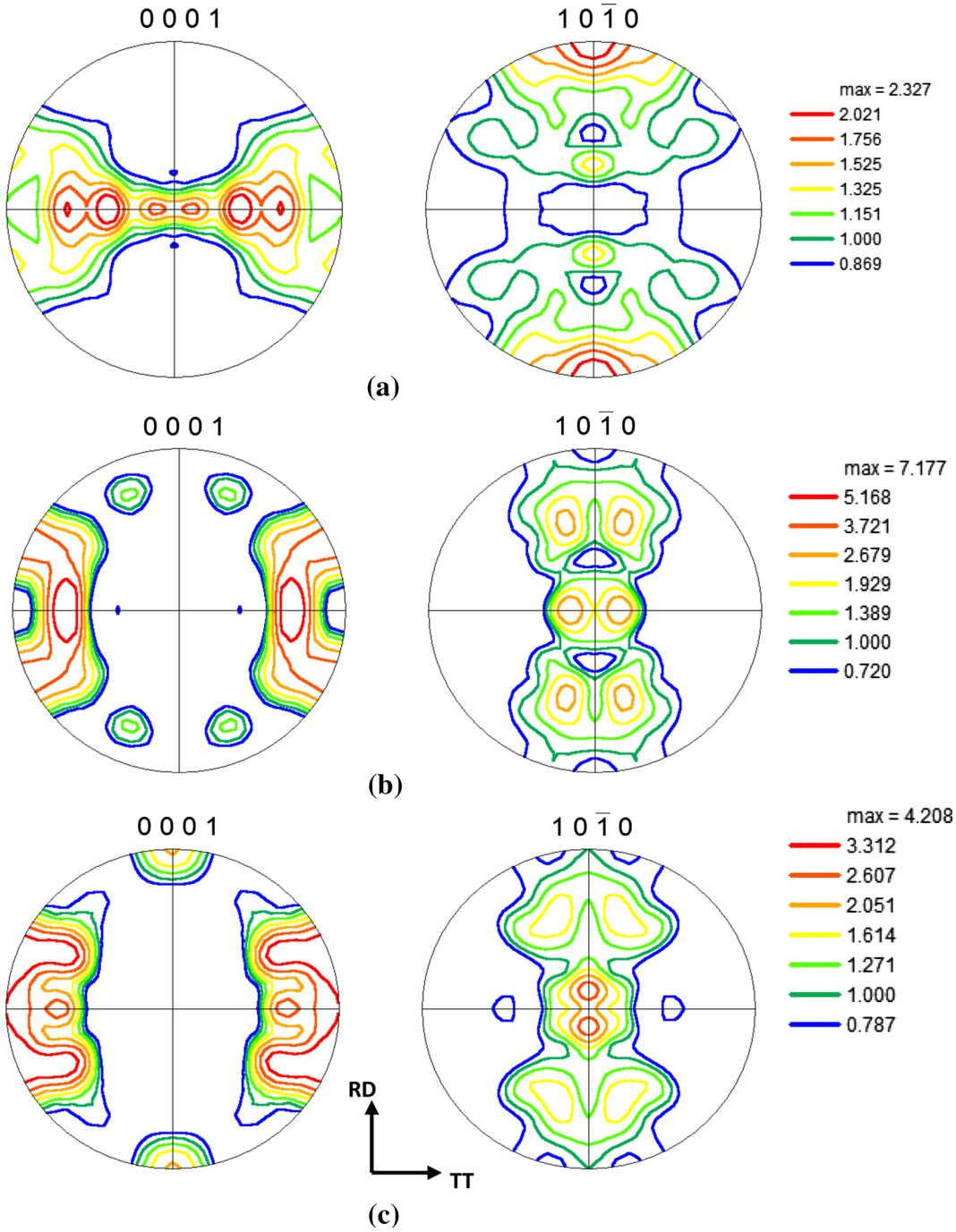

Fig. 13—Texture plots (0001) (left) and (10$\bar{1}$0) (right) of (*a*) undeformed sample, samples deformed along the TD until failure at a strain rate of (*b*) 0.01 s^{-1}, (*c*) 100 s^{-1}. Samples examined with electron beam parallel to the TD. Axis system indicates sheet orientation.

difference in the rate sensitivity of pyramidal and prismatic slip, the later being dominant in the RD and TD compression samples and also in the TD tensile samples. All 45 deg oriented samples behave as if they yield by twinning and further deformation occurs by prismatic slip. For the favorable orientation of the basal planes in the undeformed sample, basal slip does not seem to determine yielding and this is most likely a result of changes to the CRSS by alloying. The above observations also lead one to the conclusion that different alloying additions in AZ31 and ZEK100 would influence CRSS values of different slip systems differently; thus one would expect that the above observations will not be repeated in AZ31 samples even if one succeeds in preparing an AZ31 sample with a texture similar to ZEK100.

V. DISCUSSION

The measured mechanical behavior of ZEK 100 has revealed strong levels of in-plane anisotropy and

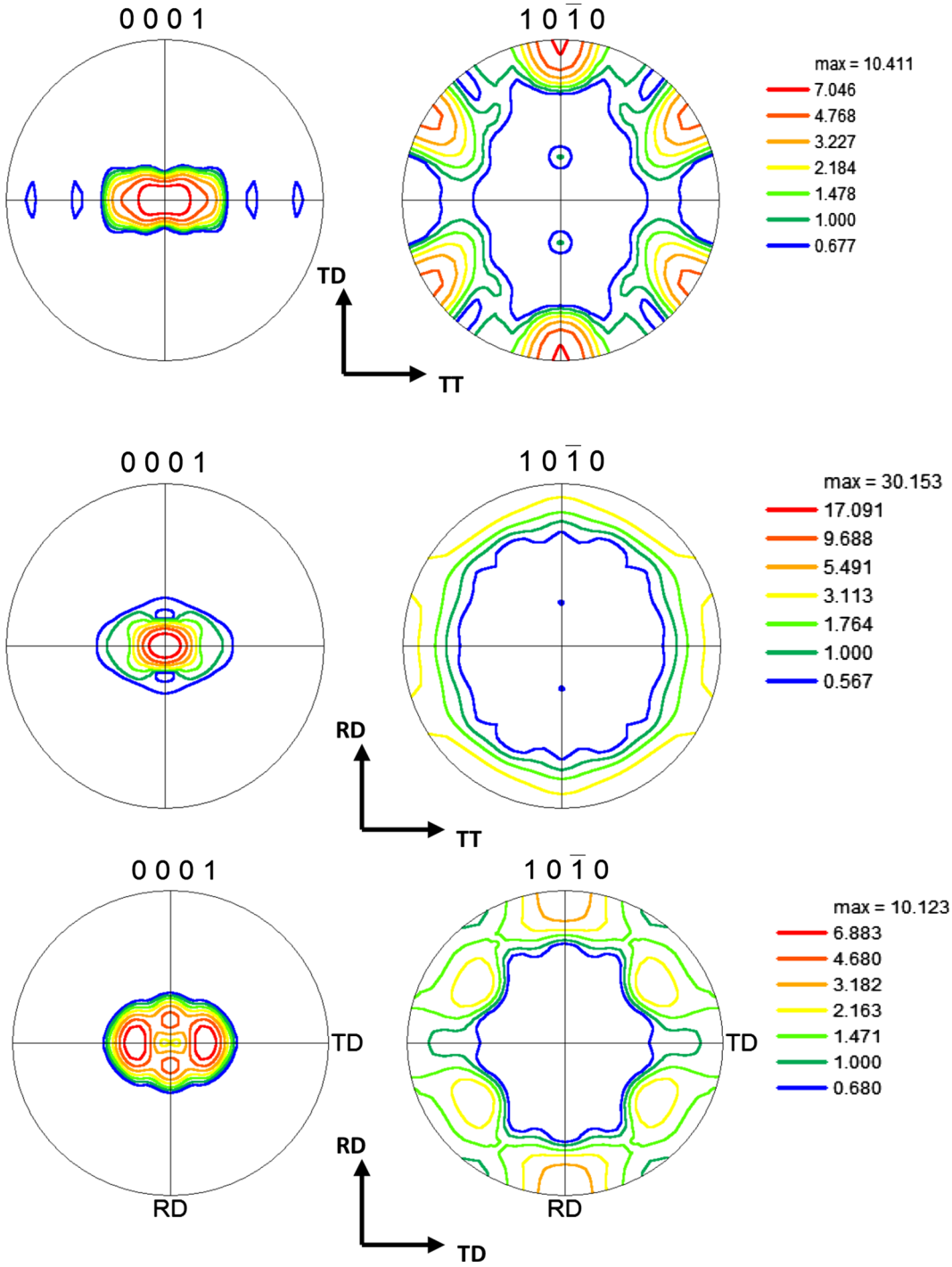

Fig. 14—Texture plots (0001) (left) and (10$\bar{1}$0) (right) of deformed compression samples at a strain rate of 0.01 s^{-1} when load axis parallel (*a*) to the RD, (*b*) to the TD, and (*c*) to the TT. Electron beam axis parallel to loading axis for each case. Axis system indicates sheet orientation.

tension–compression asymmetry, as has been previously reported for AZ31B[2,17,19,35] for example. The ZEK100 alloy also exhibits a strong dependency of strain rate sensitivity on sheet orientation that is not observed in AZ31B. Much of this mechanical response can be explained in terms of the as-received texture of the sheet material and the various operative deformation mechanisms.

The large orientation dependency in mechanical properties, especially the yield strengths, *R* values, and work hardening rates, is due to the initial crystallographic texture and, therefore, the active deformation mechanisms.[5,11,35] For instance, the texture data shown in Figure 1 shows that the *c*-axes of a considerable fraction of grains in ZEK100 are tilted toward the TD compared to commercial sheet alloys such as AZ31B.

(The *c*-axes in typical rolled AZ31B sheet are mostly parallel to the normal direction, with some tilted a few degrees toward the RD[2,5,11]). For the samples pulled along the TD, this texture in the ZEK100 sheet results initially in extension twinning followed by non-basal slip as strain increases, leading to a drop in initial yield strength and increased work hardening rates. The stress–strain response in the RD is consistent with a lack of slip systems for easy slip.[4,5,35]

The tensile rate sensitivity of the RD samples, as shown in Figure 5(a), is similar to that often exhibited by bcc metals for which yield strength is strongly rate sensitive, but hardening rate is often rate insensitive.[40] This type of behavior is also observed in commercial AZ31B rolled sheets, irrespective of sheet orientation.[2,4,11,18,35] This response is attributed to the strain rate dependency of the CRSS of the activated non-basal slip systems, as confirmed by the deformed texture data (Figure 12). In contrast, the TD and 45 deg orientations (Figures 5(b) and (c)) exhibit the opposite behavior; that is, the yield strength is lower and appears rate insensitive, while the hardening rate is strongly rate sensitive. This type of behavior is commonly observed in some fcc metals. For the ZEK100 alloy, this early deformation behavior in the TD is related to the strain rate independency of extension twinning activated in grains for which the crystallographic *c*-axes are favorably oriented toward the TD followed by the rate dependent slip activity of prismatic and pyramidal dislocations leading to high strain hardening.

To further examine the direction-dependent constitutive response of the ZEK100 sheet material, the measured tensile flow stress has been fit as a function of plastic strain and strain rate to the hcp constitutive relation given by Zerilli and Armstrong[1]:

$$\bar{\sigma} = C_0 + \left(C_1 + C_2\sqrt{\bar{\varepsilon}_p}\right)\exp\left[\left(-C_3 + C_4\ln(\dot{\varepsilon}_p)\right)T\right] + C_5\bar{\varepsilon}_p^n, \quad [1]$$

where $\bar{\varepsilon}_p$ is the effective plastic strain, $\dot{\varepsilon}_p$ is the rate of effective plastic strain, T is the absolute temperature. C_0, C_1, C_2, C_3, C_4, C_5, and n are the material constants which are determined from the experimental data. The constitutive parameters required by the Zerilli–Armstrong model (Eq. [1]) are fit to the experimental results using a non-linear regression algorithm. The measured true stress–plastic strain data at strain rates of 0.001, 0.01, 1, 10, and 1000 s^{-1} was used in the regression analysis. In the regression analysis, the plastic strain range was limited to data for which (i) the strain rate was approximately constant, and (ii) the material had not yet reached the onset of diffuse necking (stresses prior to the UTS). For each test condition, the average value of three repetitions was taken so that each experiment contributes equally to the constitutive fit and each set of experiments contain the same concentration of data points and therefore are weighted equally. It should be noted that only room temperature data was considered in the current study, so the fits will not fully capture the dependency of the material response on temperature. Table II gives the estimated values for the constitutive parameters for the RD, 45 deg and TD directions and the corresponding predicted flow curves for different strain rates are compared with the measured flow curves in Figure 15. It can be observed that good agreement with experimental results is obtained in all three directions. Note that as part of the validation process, data for strain rates of 0.1 and 100 s^{-1} was not considered in the regression and the predicted response using the calibrated material coefficients is observed to agree well with the measured data at these strain rates. The correlation coefficient and the mean absolute error for all three fits are given in Table II. The correlation coefficients all exceeded 0.985 and the mean absolute error was around 4.0 pct, both indicating that the fits are of high quality.

The approach used by Zerilli and Armstrong[1] in developing their hcp model was to combine terms from their earlier[41,42] bcc and fcc constitutive models. Zerilli and Armstrong[41,42] concluded that overcoming Peierls–Nabarro barriers, associated with dislocation motions, was the principal thermal activation mechanism for bcc metals, whereas dislocation interactions, and thus density, were the controlling mechanism for fcc metals. They viewed hcp constitutive behavior as combining aspects of both bcc and fcc strain rate sensitivity. The current ZEK100 alloy does in fact combine fcc and bcc-like response, however, the degree to which each behavior is manifest is dependent upon orientation. In Eq. [1], a bcc response is represented by material parameters C_1, C_3, and C_4, which introduce the dependency of yield strength on strain rate and temperature, while C_5 and n represent the rate- and temperature-independent work hardening typical of bcc material behavior. In the case of fcc material behavior, parameter C_0 represents a rate-insensitive yield strength, while parameters C_2 and C_4 introduce a strain rate dependent work hardening. When examining the values of the parameters fit to the measured RD response, it is seen that C_2 and C_0 are reduced to smaller values which indicate that the material when loaded along the RD behaves more like a bcc material. In contrast, in the TD and 45 deg orientations, C_1, C_5, and n are reduced to smaller values, indicating that the material behaves more like a fcc material for this loading orientation. It is noted that in the non-linear regression procedure, all of the parameters were unconstrained and simultaneously fit with the experimental data for a given orientation.

In order to develop constitutive fits to the compressive response, an alternative functional fit is required due to the twinning-slip response in compression which is very different from the tensile response. In this work, the constitutive relation proposed by Kurukuri *et al.*[2] is used to capture the in-plane compressive stress–strain response with concave upwards shape (S-shape) over the range of strain rates considered:

$$\bar{\sigma}^C = \frac{\left[K_1K_2 - \left(K_3\varepsilon_p^{K_4}\Big/1 - K_5\exp(-K_6\ln\dot{\varepsilon}_p)\right)\right]}{K_2 + \varepsilon_p^{K_4}}, \quad [2]$$

where σ^c is the equivalent stress, ε_p is the effective plastic strain, $\dot{\varepsilon}_p$ is the rate of effective plastic strain. K_1 is the initial yield strength, K_2 controls the extent of the plateau associated with the twinning regime, and K_3 is a

scaling parameter which controls the slip dominated region of the hardening curve. Parameter K_4 controls the point of inflection in the sigmoidal response. Parameters K_5 and K_6 define the strain rate dependency of the flow curve. Further description of these material parameters is given in Reference 2. The numerical values for the constitutive parameters K_1 to K_6 for the RD, TD, and 45 deg directions are given in Table III and the corresponding predicted flow curves for different strain rates are compared with the measured flow curves in Figure 16. It can be observed that good agreement with experimental results is obtained, especially in the TD and 45 deg orientations. The correlation coefficients and mean absolute errors (Table III) for the compressive fits both indicate good quality fits to the compressive data. In general, Eq. [2] accurately captures the compressive response over the range of strain rates and strains considered.

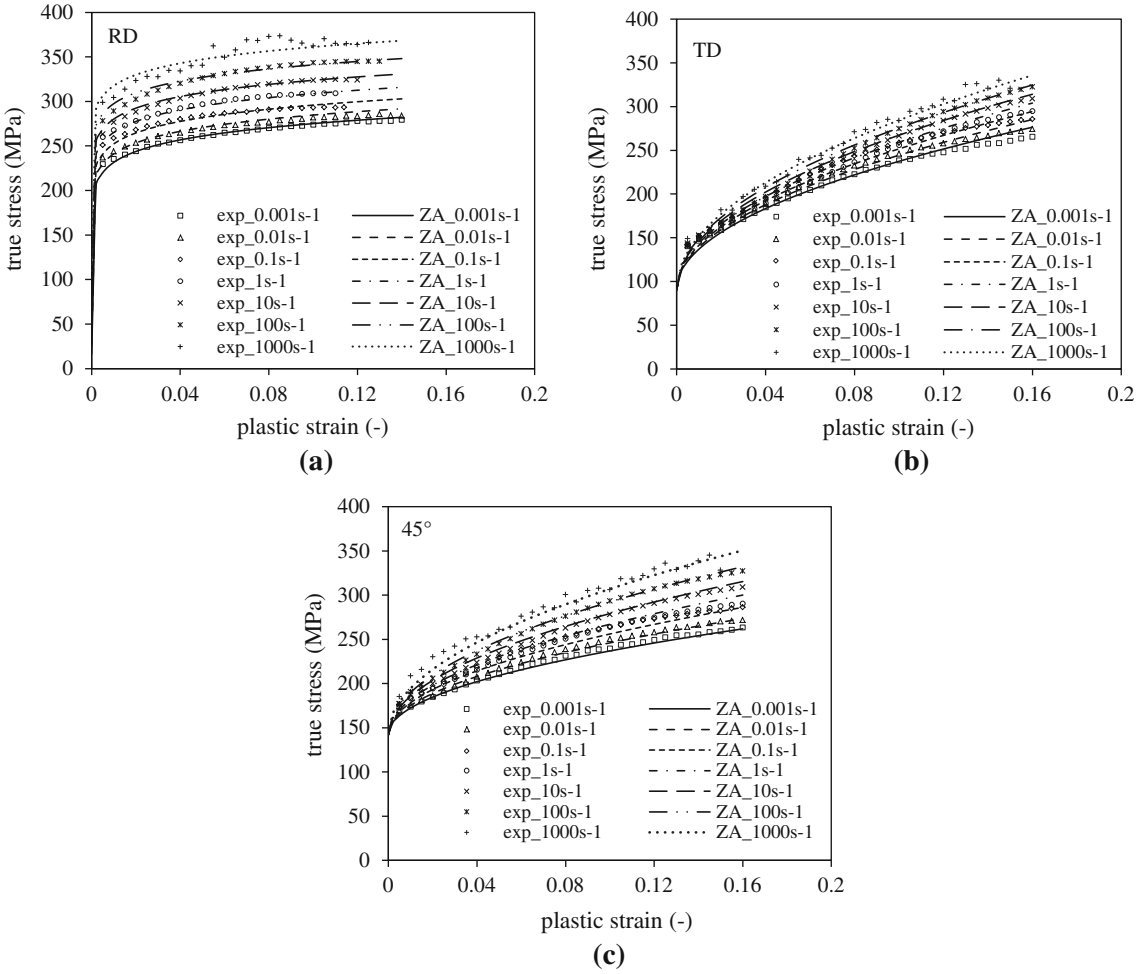

Fig. 15—Tensile true stress–plastic strain curves in the RD, TD, and 45 deg—experiments (symbols) and Zerilli–Armstrong[1] model (curves) at different strain rates.

Table II. Parameters of the Zerilli–Armstrong Model[1] for ZEK100 Sheet in Three Directions

Parameter	RD	45 deg	TD
C_0	4.711×10^{-5}	142.48	90.42
C_1	94.15	1.421×10^{-10}	9.903×10^{-11}
C_2	7.164×10^{-9}	396.28	544.46
C_3	1.013×10^{-5}	1.834×10^{-5}	6.526×10^{-5}
C_4	2.17×10^{-4}	1.357×10^{-4}	6.774×10^{-5}
C_5	269.64	9.849×10^{-8}	1.435×10^{-7}
n	0.1	5.327×10^{-8}	9.691×10^{-8}
Correlation coefficient	0.987	0.986	0.989
Mean absolute error (pct)	4.012	4.022	4.025

Table III. Parameters of the New Model[2] for Compressive Response in Three Directions

Parameter	RD	45 deg	TD
K_1	161.43	150.25	141.68
K_2	6.09×10^{-5}	9.87×10^{-3}	3.61×10^{-4}
K_3	3.86×10^{5}	6.52×10^{4}	9.55×10^{4}
K_4	6.76×10^{-6}	5.0×10^{-3}	2.4×10^{-3}
K_5	3.785	2.250	2.913
K_6	1.003	1.457	1.456
K_7	6.450×10^{-5}	8.210×10^{-3}	6.701×10^{-3}
Correlation coefficient	0.985	0.992	0.994
Mean absolute error (pct)	4.012	4.023	4.026

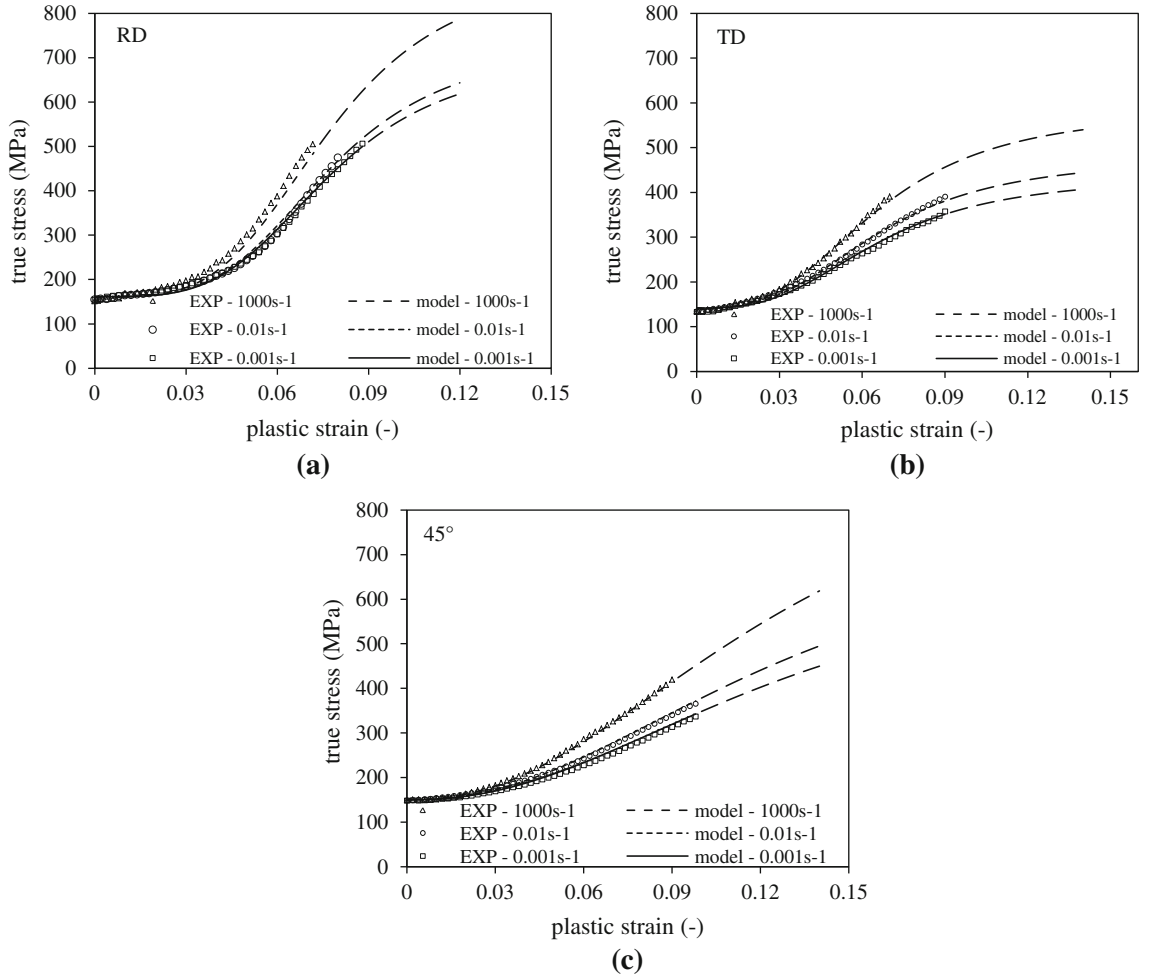

Fig. 16—Compressive true stress–plastic strain curves in the RD, TD, and 45 deg—experiments (symbols), new sigmoidal model by Kurukuri *et al.***[2] (curves), and extrapolation (long-dashed curves) at different strain rates.

The characteristics of the ZEK100 TD behavior, that is, low yield strength, high hardening rate, and high rate sensitivity, are all known to be favorable for good formability. This response is indicative of the potential advantage of the more random textures imparted by the rare-earth additions to this alloy. Clearly a magnesium alloy with these characteristics in all directions would be a desirable target for future alloy development.

VI. CONCLUSIONS

1. The ZEK100 sheet sample exhibits strong in-plane anisotropy, with significantly lower yield strength, higher hardening rates, and increased ductility as the orientation changes from the RD to TD.
2. The low to high strain rate tensile experiments reveal a significant orientation dependence of the strain rate sensitivity. In the RD, the rate sensitivity

has a significant effect on the yield strength, but a relatively mild effect on hardening rate. In the TD, the rate sensitivity has little effect on the early yield response, however, the hardening rate increases significantly with strain rate.

3. The shape of the compressive flow stress curve for the in-plane loading (RD and TD) cases is concave upward (S-shape) at all strain rates. ZEK100 sheet exhibits a lower stress level for a given strain when compressive loading is applied in the TD compared to the rolling direction. The tension–compression asymmetry in the yield stress (strength differential) is lower in the TD compared to the strong asymmetry observed in the RD.
4. The experimental tensile flow stress data has been modeled using the Zerilli–Armstrong[1] hcp constitutive model. It is observed that the orientation dependent rate sensitivity of the current material is accurately reproduced over the range of strain rates considered.
5. The constitutive equation due to[2] accurately captures the sigmoidal compressive flow stress response associated with twinning followed by slip dominated hardening over a range of strain rates. It is shown that the compressive flow stress response with the constitutive model is in good agreement with the experimental data; however, the reader is cautioned that the fits are not validated beyond the measured strain levels.

ACKNOWLEDGMENTS

This research was carried out under the framework of the Research Program of the Magnesium Network (MagNET), Canada. Financial support from General Motors of Canada, MagNET, the Canada Research Chairs Secretariat, Automotive Partnership Canada, and the Ontario Research Fund is gratefully acknowledged. The authors wish to thank Dr. Abhijit Brahme from the University of Waterloo for helpful discussions on deformation mechanisms.

REFERENCES

1. F.J. Zerilli and R.W. Armstrong: *ASME*, 1995, vol. 48, pp. 121–26.
2. S. Kurukuri, M.J. Worswick, D. Ghaffari Tari, J.T. Carter, and R.K. Mishra: *Philos. Trans. R. Soc. A*, 2014, vol. 372, p. 20130216.
3. A. Luo: *SAE Tech. Paper*, 2005, vol. 01, p. 0734.
4. J. Min, Y. Cao, J.T. Carter, and R. Verma: *Magnesium Technology*, Wiley, New York, NY, 2012.
5. S.R. Agnew and O. Duygulu: *Int. J. Plast.*, 2005, vol. 21 (6), pp. 1161–93.
6. X.Y. Lou, M. Li, R.K. Boger, S.R. Agnew, and R.H. Wagoner: *Int. J. Plast.*, 2007, vol. 23 (1), pp. 44–86.
7. S. Kurukuri, A.H. van den Boogaard, A. Miroux, and B. Holmedal: *J. Mater. Process. Technol.*, 2009, vol. 209 (15–16), pp. 5636–45.
8. D. Ghaffari Tari and M.J. Worswick: *AIP Conf. Proc.*, 2011, vol. 1353 (1), pp. 1547–52.
9. D. Ghaffari Tari, M.J. Worswick, and S. Winkler: *J. Mater. Process. Technol.*, 2013, vol. 213 (8), pp. 1337–47.
10. M. Boba, M.J. Worswick, J.T. Carter, and R.K. Mishra: *Int. Conf. on Magnesium Alloys and Their Applications*, Vancouver, BC, Canada, 2012.
11. J. Bohlen, M.R. Nürnberg, J.W. Senn, D. Letzig, and S.R. Agnew: *Acta Mater.*, 2007, vol. 55 (6), pp. 2101–12.
12. J. Bohlen, S. Yi, D. Letzig, and K.U. Kainer: *Mater. Sci. Eng. A*, 2010, vol. 527 (26), pp. 7092–98.
13. K. Hantzsche, J. Bohlen, J. Wendt, K.U. Kainer, S.B. Yi, and D. Letzig: *Scripta Mater.*, 2010, vol. 63 (7), pp. 725–30.
14. L. Jiang, J.J. Jonas, and R.K. Mishra: *Mater. Sci. Eng. A*, 2011, vol. 528 (21), pp. 6596–6605.
15. C. Dreyer, W. Chiu, R. Wagoner, and S. Agnew: *J. Mater. Process. Technol.*, 2010, vol. 210 (1), pp. 37–47.
16. T. Al-Samman and X. Li: *Mater. Sci. Eng. A*, 2011, vol. 528 (10–11), pp. 3809–22.
17. D. Hasenpouth, C. Salisbury, A. Bardelcik, and M.J. Worswick: *DYMAT*, 2009, vol. 2, pp. 1431–35.
18. D. Hasenpouth: Master's Thesis, University of Waterloo, Waterloo, ON, Canada, 2010.
19. I. Ulacia, C.P. Salisbury, I. Hurtado, and M.J. Worswick: *J. Mater. Process. Technol.*, 2011, vol. 211 (5), pp. 830–39.
20. J. Imbert and M. Worswick: *J. Mater. Process. Technol.*, 2011, vol. 211 (5), pp. 896–908.
21. J. Imbert and M. Worswick: *Mater. Process. Technol.*, 2012, vol. 212 (9), pp. 1963–72.
22. I. Ulacia, I. Hurtado, J. Imbert, C.P. Salisbury, M.J. Worswick, and A. Arroyo: *Steel Res. Int.*, 2009, vol. 80 (5), pp. 344–50.
23. T. Yokoyama: *Strain*, 2003, vol. 39 (4), pp. 167–175.
24. T. Mukai, M. Yamanoi, and K. Higashi: *Mater. Sci. Forum*, 2000, vols. 350–351, pp. 97–104.
25. E. El-Magd and M. Abouridouane: *J. Phys.*, 2003, vol. 110, pp. 15–20.
26. R. Smerd, S. Winkler, C. Salisbury, M. Worswick, D. Lloyd, and M. Finn: *Int. J. Impact Eng*, 2005, vol. 32 (1–4), pp. 541–60.
27. A.C. Thompson, C.P. Salisbury, M.J. Worswick, and R. Mayer: *J. Phys.*, 2006, vol. 134, pp. 281–86.
28. S. Kurukuri, D. Ghaffari Tari, M.J. Worswick, J.T. Carter, and R.K. Mishra: *Int. Conf. on Magnesium Alloys and Their Applications*, Vancouver, BC, Canada, 2012.
29. D. Ghaffari Tari, M.J. Worswick, U. Ali, and M. Gharghouri: Unpublished research, 2013.
30. A. Bardelcik, M. Worswick, S. Winkler, and M. Wells: *Int. J. Impact Eng.*, 2012, vol. 50, pp. 49–62.
31. C.P. Salisbury: Master's Thesis, University of Waterloo, Waterloo, ON, Canada, 2001.
32. A. Bardelcik, C.P. Salisbury, S. Winkler, M. Wells, and M.J. Worswick: *Int. J. Impact Eng.*, 2010, vol. 37 (6), pp. 694–702.
33. C. Mason and M.J. Worswick: *Int. J. Fract.*, 2001, vol. 111, pp. 29–51.
34. A. Bardelcik: Private communication, 2013, University of Waterloo, Waterloo, Canada.
35. I. Ulacia, N. Dudamell, F. Gálvez, S. Yi, M. Pérez-Prado, and I. Hurtado: *Acta Mater.*, 2010, vol. 58 (8), pp. 2988–98.
36. M.R. Barnett: *Metall. Mater. Trans. A*, 2003, vol. 34A, pp. 1799–1806.
37. Y. Chino, M. Kado, and M. Mabuchi: *Mater. Sci. Eng. A*, 2008, vol. 494 (1–2), pp. 343–49.
38. S. Yi, J. Bohlen, F. Heinemann, and D. Letzig: *Acta Mater.*, 2010, vol. 58 (2), pp. 592–605.
39. A.S. Khan, A. Pandey, T. Gnäupel-Herold, and R.K. Mishra: *Int. J. Plast.*, 2011, vol. 27 (5), pp. 688–706.
40. R.W. Armstrong and S.M. Walley: *Int. Mater. Rev.*, 2008, vol. 53 (3), pp. 105–28.
41. F.J. Zerilli and R.W. Armstrong: *J. Appl. Phys.*, 1987, vol. 61 (5), pp. 1816–25.
42. F.J. Zerilli and R.W. Armstrong: *Acta Metall. Mater.*, 1992, vol. 40 (8), pp. 1803–08.